INORGANIC CHEMISTRY
FRONTIERS

CHINESE CHEMICAL SOCIETY

ROYAL SOCIETY OF CHEMISTRY

RESEARCH ARTICLE

View Article Online
View Journal | View Issue

Check for updates

Cite this: *Inorg. Chem. Front.*, 2022, **9**, 5950

Coordination site manipulation of the annular growth mechanism to assemble chiral lanthanide clusters with different shapes and magnetic properties†

Bing-Fan Long,[a] Shui Yu,[a] Zhong-Hong Zhu, *[a] Yun-Lan Li,[a] Fu-Pei Liang*[a,b] and Hua-Hong Zou *[a]

Received 6th August 2022,
Accepted 25th September 2022

DOI: 10.1039/d2qi01711c

rsc.li/frontiers-inorganic

Chiral lanthanide clusters provide a platform for molecular-based materials with coordination between chirality and magnetism and exhibit great application prospects in the fields of three-dimensional displays, magneto-optical memories, and spintronic devices. To date there is no reliable self-assembly rule for the directional design of chiral lanthanide clusters with specific shapes and functions. Further, we are the first to achieve the directional construction of chiral lanthanide clusters with different shapes and magnetic properties by regulating the hydroxyl coordination sites at different positions on the ligands by manipulating the annular growth mechanism. Specifically, we carried out the reaction of ***R*/*S***-mandelic acid hydrazide, 2,5-dihydroxybenzaldehyde and $DyCl_3·6H_2O$ with methanol and water as mixed solvents under solvothermal conditions at 80 °C to obtain mutual enantiomers tetranuclear chiral lanthanide clusters ***R*/*S*-1**. In ***R*/*S*-1**, first, two HL^1 ligands captured one Dy(III) ion to form a template unit $Dy(L^1)_2$, and following this, four $Dy(L^1)_2$ template units were well-ordered and arranged at the four vertices of the square, which were induced by a bridge anion μ_4-O^{2-}, to undergo the annular growth mechanism to form square-shaped clusters ***R*/*S*-1**. Replacing 2,5-dihydroxybenzaldehyde with 2,3,4-trihydroxybenzaldehyde in the reaction system, hexanuclear chiral clusters ***R*/*S*-2** were obtained. Changing the hydroxyl coordination sites enabled one H_3L^2 ligand to capture two Dy(III) ions, forming a template unit Dy_2L^2, following which three Dy_2L^2 were connected by a μ_3-OH^- bridge anion along the annular growth to form a triangular pyramid-shaped hexanuclear chiral lanthanide cluster ***R*/*S*-2**. Circular dichroism spectra indicated that ***R*/*S*-1** and ***R*/*S*-2** were two pairs of enantiomers. Magnetic studies showed that the ***R*-1** chiral cluster was a typical single-molecule magnet under a zero dc field, and it exhibited a distinct double relaxation behavior. To the best of our knowledge, this is one of the rare examples of chiral lanthanide clusters with double relaxation behavior. This work provides an effective method for the directional construction of chiral lanthanide clusters with different connections and shapes and opens up a new horizon for the design and synthesis of multifunctional materials with magneto-optical applications.

Introduction

Chirality is a fundamental property of nature that plays a very vital role in connecting micro and macro molecules, and it is closely related to the origin of life.[1–3] The formation of biological macromolecules in nature, such as the double helix structure of DNA, nucleic acids and proteins of their hierarchical structure is all derived from the regulation of chirality.[4–6] However, the study of these chiral macromolecules is very complicated and difficult to effectively elaborate through specific single crystal structures.[7–9] Therefore, there is an urgent need to develop some simple and effective simplified models to facilitate the exploration of the formation process of chiral macromolecules. Chiral nanoclusters with precise structural

---

[a] *School of Chemistry and Pharmaceutical Sciences, State Key Laboratory for Chemistry and Molecular Engineering of Medicinal Resources/Key Laboratory for Chemistry and Molecular Engineering of Medicinal Resources (Ministry of Education of China), Collaborative Innovation Center for Guangxi Ethnic Medicine, School of Chemistry and Pharmaceutical Sciences, Guangxi Normal University, Guilin 541004, P. R. China. E-mail: 18317725515@163.com, liangfupei@glut.edu.cn*

[b] *Guangxi Key Laboratory of Electrochemical and Magnetochemical Functional Materials, College of Chemistry and Bioengineering, Guilin University of Technology, Guilin 541004, P. R. China. E-mail: gxnuchem@foxmail.com*

† Electronic supplementary information (ESI) available. CCDC 2194449–2194452. For ESI and crystallographic data in CIF or other electronic format see DOI: **https://doi.org/10.1039/d2qi01711c**

connections and compositions as simplified models have established an efficient platform for the study of complex chiral compounds.[10–12] In addition, chiral nanoclusters have shown wide application prospects in asymmetric catalysis, enantioselective recognition, circularly polarized luminescent materials, biomimetic chemistry, molecular magnetism, *etc.*[13–18] In 2017, Cui *et al.* reported a chiral porous octahedral cage, which can serve as an efficient asymmetric supramolecular catalyst and achieve high catalytic activity and high selectivity.[19] In 2021, Zhou *et al.* prepared a chiral dodecanuclear lanthanide double-shell porous coordination cage and extended its use for the selective separation of racemic enantiomers.[20] Chiral lanthanide clusters as an important part of chiral nanoclusters have both chirality and magnetism and have shown great application prospects in magnetic chiral dichroism (MchD), circularly polarized luminescence (CPL), second harmonic generation (SHG) and other aspects.[21–23] In 2019, Tong *et al.* reported a pair of dinuclear chiral erbium-based single-molecule magnets and studied their magnetic structure relationship.[24]

Due to the variable coordination numbers, weak stereochemical bias and kinetic instability of lanthanide ions, research on the formation process and self-assembly mechanism of lanthanide clusters has been slow.[25–27] Although the exploration of the self-assembly mechanism of lanthanide clusters is still at the initial stage, we have made a series of progresses in this field.[28–37] In 2018, we were the first to use HRESI-MS to track the self-assembly process of triangular-shaped dysprosium clusters with toroidal magnetic moments.[28] Furthermore, we were the first to use crystallography combined with the HRESI-MS technique to trace the formation mechanism of the high-nuclearity lanthanide cluster Dy_{10} with double relaxation behavior.[29] In 2020, the ligand chelation method was first proposed to construct the largest double cage-like cluster Dy_{60} and its intermediate Dy_{30} was obtained.[30] In addition, we achieved the construction of the caged lanthanide cluster Dy_{14} using strong hydrogen bonding of the dish-shaped cluster precursors and achieved a highly selective photoresponse to heavy metal ions in the solution.[31] In 2021, we were the first to propose the out-to-in growth mechanism to guide the directional construction of a series of 16 nuclear dish-like lanthanide clusters, and under the guidance of the above mechanism, a series of different types of lanthanide clusters were obtained by changing the reaction conditions.[32] Such as crown-shaped high-nucleation lanthanide cluster Dy_{34} *etc.*[33] Recently, we have successfully constructed the largest series of brucite-like dysprosium-based nanoclusters of Dy_{19} under solvothermal reactions, and proposed their possible assembly mechanisms as the in-plane growth mechanism or planer epitaxial growth mechanism.[38] The introduction of chirality into lanthanide clusters will complicate the formation process. Therefore, the research on the formation process and self-assembly mechanism of chiral lanthanide clusters is still blank.

Herein, two pairs of chiral lanthanide clusters ***R*/*S*-1** (Scheme 1a) and ***R*/*S*-2** (Scheme 1b), which are enantiomers of each other, were obtained by controlling the coordination sites of acylhydrazone ligands and reaction with Dy(III) ions under solvothermal conditions. Specifically, the chiral ***R*/*S***-mandelic acid hydrazide, 2,5-dihydroxybenzaldehyde, and $DyCl_3·6H_2O$ were used as raw materials, and with MeOH and H_2O as mixed solvents were reacted under solvothermal conditions to obtain square-shaped chiral clusters ***R*/*S*-1** by the assembly of eight ***R*/*S***-HL^1 ligand molecules and four Dy(III) ions. After replacing 2,5-dihydroxybenzaldehyde with 2,3,4-trihydroxybenzaldehyde with more aggregated coordination sites, a pair of triangular pyramidal chiral hexanuclear lanthanide clusters ***R*/*S*-2** were obtained. The regulation of the coordination sites of the reaction starting materials leads to the formation of the template

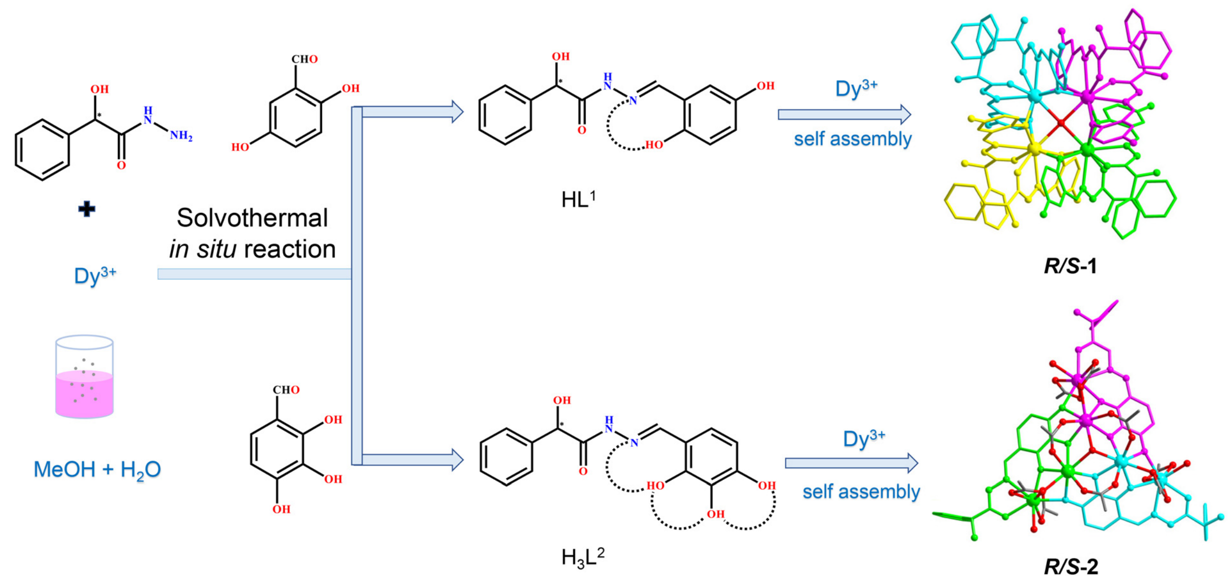

Scheme 1 Synthetic schematic diagram of clusters ***R*/*S*-1** and ***R*/*S*-2**.

units of the two pairs of enantiomers with different structural connections ($Dy(L^1)_2$ and Dy_2L^2), and then the different template units form chiral clusters with different shapes through the annular growth mechanism. To the best of our knowledge, this is the first time that chiral lanthanide clusters with different linkages and shapes have been constructed by regulating the coordination sites on the ligands. Magnetic studies showed that ***R*-1** was a single-molecule magnet with double relaxation behaviors under zero fields, and ***R*-2** had obvious frequency-dependent behaviors under zero fields. This work provides a vivid example for the design and synthesis of chiral lanthanide clusters and opens a door for the directed synthesis of multifunctional materials with magneto-optical applications.

Results and discussion

Structural analysis of *R*/*S*-1 and *R*/*S*-2

Accurately weighed ***R*/*S***-mandelic acid hydrazide (0.1 mmol, 0.0166 g), 2,5-dihydroxybenzaldehyde (0.1 mmol, 0.0138 g) and $DyCl_3·6H_2O$ (0.5 mmol, 0.1885 g) were reacted in the mixed solvents of methanol and water (0.8 : 0.4 mL) under solvothermal conditions at 80 °C, which gave rise to a light green bulk crystal ***R*/*S*-1**. Single-crystal XRD (SCXRD) data indicated that the ***R*/*S*-1** crystallized in the orthorhombic space group *I*222 (Table S1†). The structures of ***R*-1** and ***S*-1** were a pair of enantiomeric structures and ***R*-1** was discussed in detail. To be specific, the structure framework of ***R*-1** contains four Dy(III) ions, eight deprotonated *R*-(*E*)-*N*′-(2,5-dihydroxybenzylidene)-2-hydroxy-2-phenyl-2λ^3-ethanehydrazide (R-$(L^1)^-$) ligands, one bridged anion μ_4-O^{2-}, two peripherally free Cl^- anions, eight peripherally free MeOH molecules and twelve peripherally free H_2O molecules. The molecular formula of ***R*-1** was $[Dy_4(L^1)_8(\mu_4\text{-}O)]·2Cl·xCH_3OH·yH_2O$ (***R*-1**: $x = 8$, $y = 12$; ***S*-1**: $x = 3$, $y = 7$) (Fig. 1a and b). The independent unit of ***R*-1** consists of one Dy(III) ion and two deprotonated R-$(L^1)^-$ ligands. First, the two R-$(L^1)^-$ ligand units chelated one Dy(III) ion in a crossover pattern, forming a $Dy(L^1)_2$ fragment (Fig. 3a, ***S*-1** shown in Fig. S1a†). Subsequently, the four $Dy(L^1)_2$ units arranged on the four vertices of the square by an annular arrangement and are further bridged by an anion μ_4-O^{2-} to form a square-shaped tetranuclear dysprosium cluster ***R*-1** (Fig. 1c and d). The {Dy/O} nuclei of ***R*-1** exhibited a square arrangement (Fig. 1e and f). Furthermore, the eight ligands R-$(L^1)^-$ in the cluster ***R*-1** exhibited the same coordination pattern: μ_2-η^1:η^1:η^2 (Fig. 3b, ***S*-1** shown in Fig. S1b†). All the metal center Dy(III) ions were in a ninth-coordinated O_7N_2 coordination environment by the R-$(L^1)^-$ ligands and the bridged anion μ_4-O^{2-}. The coordination configuration of the metal center Dy(III) ion was calculated using SHAPE software to be a capped square antiprism (CSAPR-9) (Fig. 3c, ***S*-1** shown in Fig. S1c, and Tables S6 and S7†).[39] The structural analysis showed that the bond lengths between Dy–O and Dy–N in ***R*/*S*-1** were in the normal range (Tables S2 and S3†).

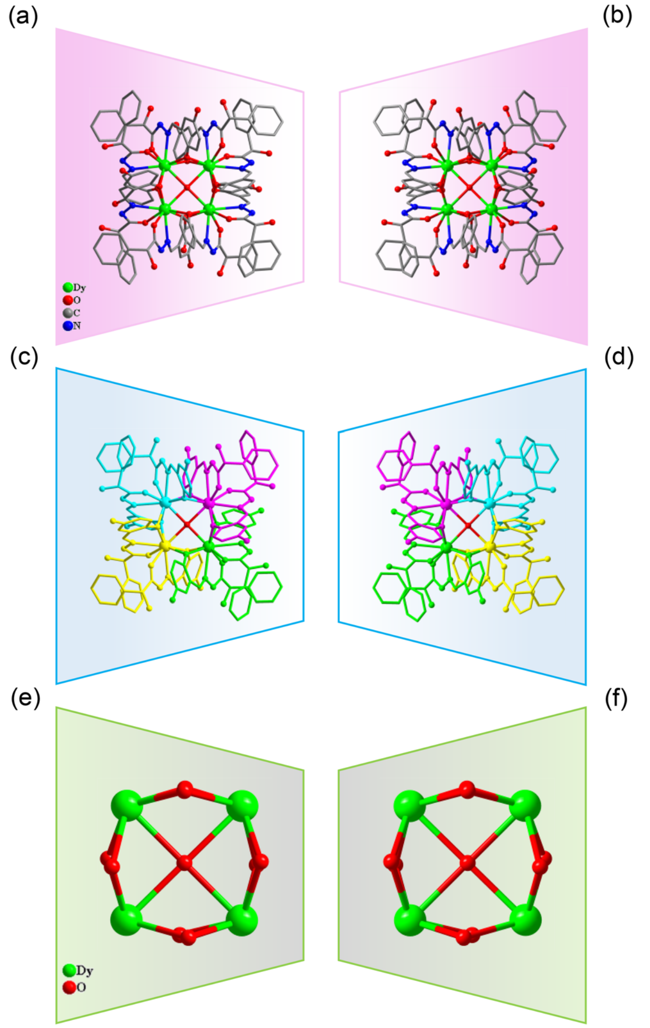

Fig. 1 Structure of ***R*/*S*-1** (a and b); four $Dy(L^1)_2$ fragments of ***R*/*S*-1** (c and d); and cluster core connection (e and f).

When we replaced 2,5-dihydroxybenzaldehyde with 2,3,4-trihydroxybenzaldehyde (0.1 mmol, 0.0154 g), the metal salt was changed to $Dy(OAc)_3·4H_2O$ (0.5 mmol, 0.2058 g) under the same reaction conditions and two yellow bulk crystals ***R*/*S*-2** were obtained. SCXRD results showed that the clusters ***R*-2** and ***S*-2** were a pair of enantiomers crystallized in the monoclinic system *I*2 space group (Table S1†). Here, the structure of ***R*-2** was discussed in detail. The ***R*-2** was composed of six Dy(III) ions, three *R*-deprotonated(*E*)-2-hydroxy-2-phenyl-*N*′-(2,3,4-trihydroxybenzylidene)-2λ^3-ethanehydrazide (R-$(L^2)^{3-}$) ligands, one bridged anion μ_3-OH^-, nine terminally coordinated OAc^-, three terminally coordinated H_2O molecules, one peripherally free H_3O^+ ion, six peripherally free MeOH molecules and three peripherally free H_2O molecules. The molecular formula of ***R*-2** was $[Dy_6(L^2)_3(\mu_3\text{-}OH)(OAc)_9(H_2O)_3]·H_3O·xCH_3OH·yH_2O$ (***R*-2:** $x = 6$, $y = 3$; ***S*-2:** $x = 4$, $y = 2$) (Fig. 2a and b). The smallest asymmetric unit of ***R*-2** consists of two Dy(III) ions and one deprotonated organic ligand R-$(L^2)^{3-}$. Interestingly, we regulated the position of the hydroxyl coordination sites on the reaction starting materials. That is, the change from 5-hydroxyl to 3-hydroxyl resulted in more concentrated chelation sites for

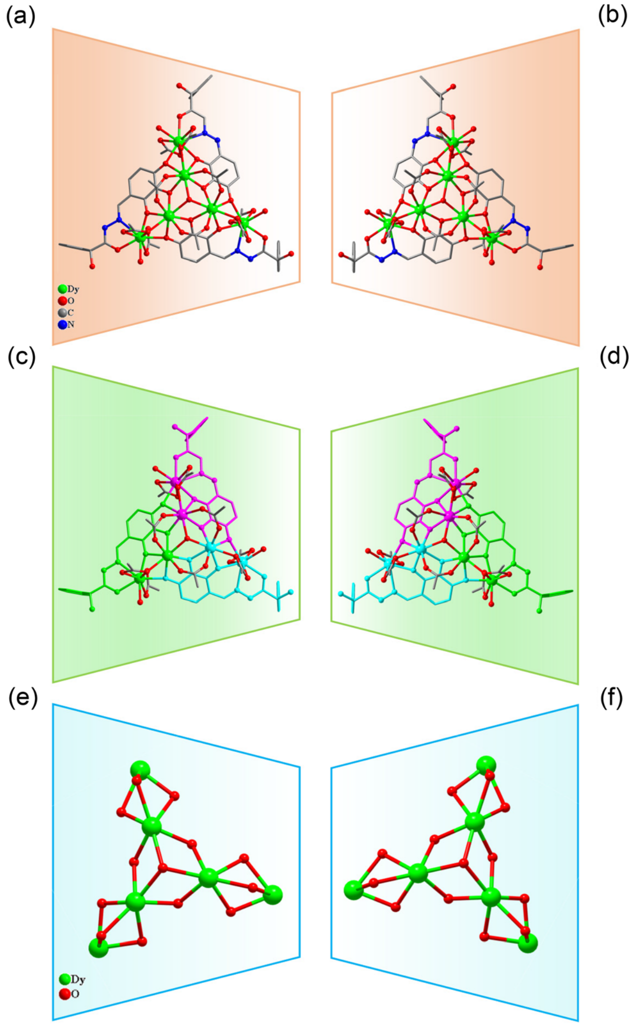

Fig. 2 Structure of ***R*/*S*-2** (a and b); three Dy$_2$L^2 fragments of ***R*/*S*-2** (c and d); and cluster core connection (e and f).

R-(L^2)$^{3-}$. Therefore, *R*-(L^2)$^{3-}$ can effectively capture two Dy(III) ions to form a Dy$_2$L^2 template unit at the initial stage of the reaction (Fig. 3d, ***S*-2** shown in Fig. S1d†). Furthermore, the added coordination sites of 4-hydroxyl on the *R*-(L^2)$^{3-}$ ligand can further bridge the Dy$_2$L^2 template unit of another molecule, finally forming a triangular pyramid-shaped hexanuclear cluster ***R*-2** (Fig. 2c and d). The cluster core {Dy/O} of ***R*-2** contains three Dy$_2$O$_5$ connected by an anion μ_3-OH$^-$ (Fig. 2e and f). The three ligands in the cluster ***R*-2** had the same coordination mode as μ_4-η^1:η^1:η^2:η^2:η^2 (Fig. 3e, ***S*-2** shown in Fig. S1e†). The metal center Dy(III) ions had two different coordination environments. The metal center Dy1 was surrounded by an O$_8$N$_1$ coordination environment formed by *R*-(L^2)$^{3-}$, OAc$^-$ and terminally coordinated H$_2$O molecules and its coordination configuration was calculated using SHAPE to be a capped square antiprism (CSAPR-9) (Fig. 3f, ***S*-2** shown in Fig. S1f†). The Dy2 was surrounded by an O$_8$ coordination environment formed by *R*-(L^2)$^{3-}$, OAc$^-$ and bridged anion μ_4-O^{2-} and its coordination configuration was biaugmented trigonal prism (BTPR-8) (Fig. 3g, ***S*-2** shown in Fig. S1g, and Tables S8 and S9†). The structural analysis showed that the bond lengths between Dy–O and Dy–N in ***R*/*S*-2** were in the normal range (Tables S4 and S5†).

The clusters ***R*/*S*-1** (Fig. S2a†) and ***R*/*S*-2** (Fig. S2b†) were two pairs of enantiomers, so they have similar infrared absorption peaks. The test results showed that they all have characteristic absorption peaks including ν(HO–H) of the water molecule, C═N of the imine group (–C═N–), C═N and C═C of the aromatic ring, and C–O of the phenolic hydroxyl group.[40] The thermogravimetric curves of ***R*/*S*-1** and ***R*/*S*-2** showed that the frameworks were stable up to 180 °C, after which they quickly collapsed. From 35 to 170 °C, the weight loss of ***R*-1** was 13.42%, which corresponds to eight free MeOH molecules and twelve free H$_2$O molecules (theoretical, 13.09%) (Fig. S3a†). The weight loss of ***S*-1** was 6.87% from 35 to 170 °C, which

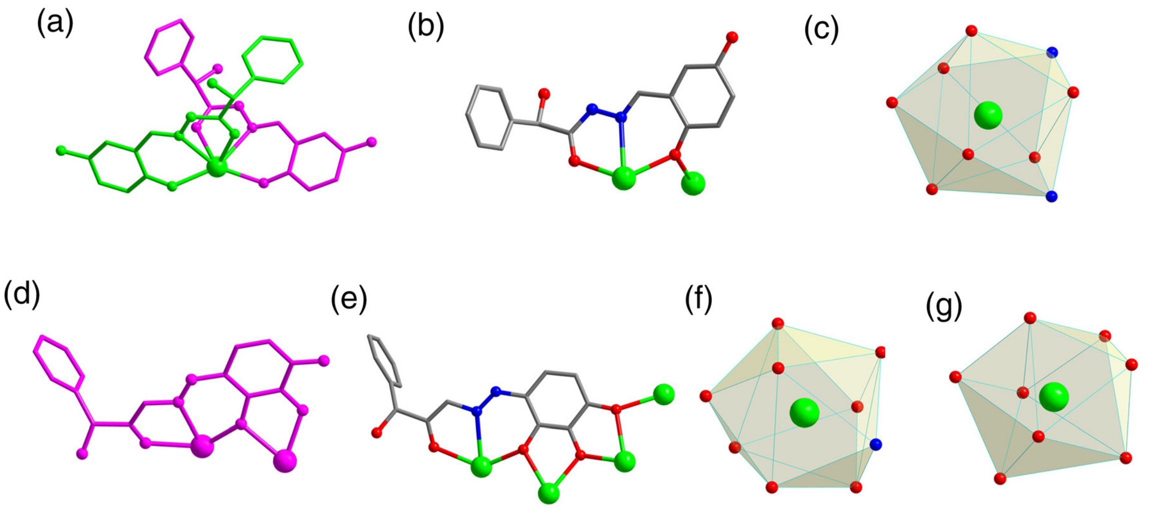

Fig. 3 The asymmetric unit of ***R*-1** (a) and ***R*-2** (d); ligand coordination mode of ***R*-1** (b) and ***R*-2** (e); and coordination polyhedron around the Dy(III) ions of ***R*-1** (c) and ***R*-2** (f and g).

corresponds to three free MeOH molecules and seven free H_2O molecules (theoretical, 6.59%) (Fig. S3b†). From 35 to 180 °C, the weight loss of ***R*-2** was 11.85%, which corresponds to six free MeOH molecules and four free H_2O molecules and three terminally coordinated H_2O molecules (theoretical, 13.25%) (Fig. S3c†). For the ***S*-2**, the weight loss rate was 9.52% over the range 35–180 °C, which corresponds to the loss of four free MeOH molecules, three free H_2O molecules and three terminally coordinated H_2O molecules (theoretical, 8.69%) (Fig. S3d†). Powder X-ray diffraction (PXRD) patterns of ***R*/*S*-1** and ***R*/*S*-2** (Fig. S4†) agreed well with simulated patterns calculated from SCXRD data, indicating phase purity in all crystalline samples.

As for ***R*/*S*-1**, first, two HL^1 ligand molecules captured one Dy(III) ion, forming the template unit $Dy(L^1)_2$. And then four $Dy(L^1)_2$ template units were well-ordered arranged at the four vertices of the square to form a square-like tetranuclear cluster ***R*/*S*-1** by a bridged anion μ_4-O^{2-} (Scheme 2a). In the process of ***R*/*S*-1** formation, the template unit $Dy(L^1)_2$ undergoes a hydrolysis-induced annular growth mechanism to form the final product. When we changed the coordination sites on the aldehyde, the original 5-hydroxyl was changed to 3-hydroxyl, which resulted in more aggregation of the coordination sites on the ligand. One H_3L^2 ligand molecule can capture two Dy(III) ions, forming the template unit Dy_2L^2. Furthermore, the above-mentioned multiple template units Dy_2L^2 were then bridged by an anion μ_3-OH^- to form triangular pyramid-like hexanuclear clusters ***R*/*S*-2** (Scheme 2b). In a word, we obtained template units with different linkages by regulating the coordination sites of ligands and achieved the manipulation of the annular growth mechanism to construct chiral lanthanide clusters with different shapes and linkages.

CD spectra analysis of *R*/*S*-1 and *R*/*S*-2

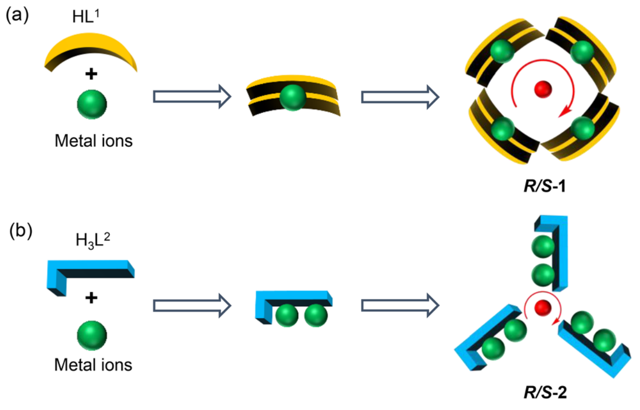

Scheme 2 Schematic diagrams of growth mechanisms of the ***R*/*S*-1** (a) and ***R*/*S*-2** (b).

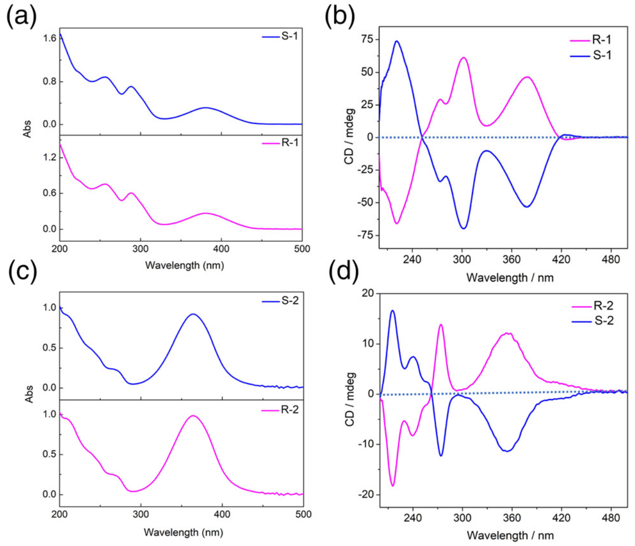

Fig. 4 The UV-vis absorption spectra of clusters ***R*/*S*-1** (a) and ***R*/*S*-2** (c). CD spectra of clusters ***R*/*S*-1** (b) and ***R*/*S*-2** (d).

The chiral optical activity and enantiomeric characteristics of clusters ***R*/*S*-1** and ***R*/*S*-2** were verified by circular dichroism (CD) spectra in methanol. The CD signal peaks of the two enantiomers at a concentration of 0.1 g L^{-1} in the range of 200–500 nm presented a nearly perfect mirror symmetry (Fig. 4b and d). The results indicated that ***R*-1** displayed a strong positive Cotton effect at 242 and 303 nm, a weak positive Cotton effect at 273 nm and a strong negative Cotton effect at 221 nm, while ***S*-1** showed opposite signals at the same wavelength to form a mirror image, indicating that ***R*-1** and ***S*-1** were a pair of enantiomers. The CD signals of ***R*/*S*-2** were different from those of the ***R*/*S*-1** due to the significant difference in self-assembled structure. The ***R*-2** exhibited a strong positive Cotton effect at 354 nm and 273 nm, a weak negative Cotton effect at 240 nm and a strong negative Cotton effect at 215 nm, while ***S*-2** showed opposite signals at the same wavelength, confirming that the ***R*-2** and ***S*-2** were a pair of enantiomers. In combination with the absorption spectrum analysis, the ***R*/*S*-1** had three strong absorption peaks at 380 nm, 288 nm and 256 nm, which were attributed to the n–π* transition of the imino group on the ligands and the π–π* transition of the aromatic group (Fig. 4a). The ***R*/*S*-2** had a strong absorption peak at 364 nm, which was attributed to the n–π* transition of the imino group and the π–π* transition of the aromatic group, while a weak shoulder peak at 271 nm was attributed to the π–π* transition on the ligands (Fig. 4c).[41,42]

Magnetic analysis of clusters *R*/*S*-1 and *R*/*S*-2

The variable-temperature molar magnetic susceptibility of clusters ***R*/*S*-1** and ***R*/*S*-2** was measured from 300 K to 2 K under an external dc magnetic field of 0.1 T.[43–47] The $\chi_m T$ values of clusters ***R*-1**, ***S*-1**, ***R*-2** and ***S*-2** were 55.17, 55.95, 85.13 and 85.96 cm^3 mol^{-1} K at 300 K, respectively, which were close to expected values ($^6H_{15/2}$, $S = 5/2$, $g = 4/3$, $J = 15/2$, $L = 5$) (Fig. S5a, S8a, S5b and S8b†). The $\chi_m T$ values of clusters ***R*-1** and ***S*-1** reached minimum values of 46.69 cm^3 mol^{-1} K and 50.92 cm^3 mol^{-1} K at 14 K, which can be attributed to the thermal depopulation of the excited Stark sublevels of Dy(III) ions. Then the ***R*-1** increased to 49.75 cm^3 mol^{-1} K and the ***S*-1** reached 53.94 cm^3 mol^{-1} K at 2 K, which can be attributed to a weak ferromagnetic interaction. For the ***R*-2** and ***S*-2**, the $\chi_\mathrm{m}T$ values decreased and reached the minimum values of 42.44 cm^3 mol^{-1} K and 44.37 cm^3 mol^{-1} K at 2 K, which was likely due to the presence of intermolecular weak antiferromagnetic coupling. The magnetization *versus* magnetic field plots of clusters ***R*/*S*-1** and ***R*/*S*-2** in the applied field of 0–7 T and temperature range of 2–5 K, respectively. The magnetization of clusters ***R*-1**, ***S*-1**, ***R*-2** and ***S*-2** was 18.92, 17.75, 27.16 and 34.23$N\beta$, respectively. The nonoverlapping M *versus* HT^{-1} graph revealed the existence of significant magnetic anisotropy which may be attributed to the strong crystal field effect (Fig. S5c, S8c, S5d and S8d†). Furthermore, the hysteresis loops of clusters ***R*-1**, ***S*-1**, ***R*-2** and ***S*-2** were not obvious at 2 K which may be caused by the strong quantum tunneling effect of Dy(III) ions (Fig. S6a, S9a, S6b and S9b†).

To further study the magnetic relaxation dynamics of clusters ***R*/*S*-1** and ***R*/*S*-2**, we conducted alternating current (AC) magnetization under zero dc field at different temperatures in the frequency range of 10–999 Hz. The results indicated that the in-phase (χ') and out-of-phase (χ'') AC susceptibilities of ***R*-1** and ***S*-1** had obvious frequency and temperature dependence, which confirmed that ***R*-1** and ***S*-1** showed slow magnetic relaxation behavior. Also the out-of-phase signal had a distinct peak of ***R*-1** and ***S*-1**, and with the increase of frequency, the peak gradually shifted to the high temperature region, which was a typical feature of SMMs (Fig. 5a and S10a†). The field-dependence of magnetic dynamics was monitored at 2 K (Fig. S11a and S11b†) for ***R*-1** and ***S*-1**, respectively. The field-dependence of the relaxation time τ indicates that the relaxation rate decreases to a minimum under the applied dc field of 1000 Oe (Fig. S11c and S11d†). Therefore, 1000 Oe was selected as an optimum external dc field for further measurements of ***R*-1** and ***S*-1**. We found that the quantum tunneling effect can be suppressed. Both in-phase and out-of-phase signals of clusters ***R*-1** and ***S*-1** showed obvious peaks (Fig. S11e and S11f†). For the ***R*-2** and ***S*-2**, only a slight frequency-dependent behavior was observed, and no obvious peak was observed with the decreasing temperature, which might be caused by the fast quantum tunneling effect of the clusters ***R*-2** and ***S*-2** at low temperature (Fig. 5c and S13a†). When a certain external field was applied, the quantum tunneling effect might be suppressed. Therefore, the ***R*-2** and ***S*-2** were tested under 1000 Oe external dc field. In order to study the magnetic behavior of ***R*-2** and ***S*-2** under 1000 Oe dc fields, the in-phase and out-of-phase AC susceptibilities were plotted as a function of temperature (χ'/χ'' *vs.* T) (Fig. S7a and S13b†) and frequency (χ'/χ'' *vs.* ν), respectively (Fig. S7b and S7c†). The results showed that the in-phase and out of phase only showed slight frequency dependence, no peak. Although an external field of 1000 Oe was applied, the experimental results showed that the in-phase and out of phase signals of ***R*-2** and ***S*-2** were not significantly different from under zero field, confirming that ***R*-2** and ***S*-2** had no field effect, and only exhibited frequency-dependent behavior.

To explore the relaxation process of ***R*-1** and ***S*-1**, the Cole–Cole diagram between 2 K and 12 K was fitted and the fitting values were basically consistent with the generalized Debye model. The ***R*-1** and ***S*-1** presented two semicircular shapes,

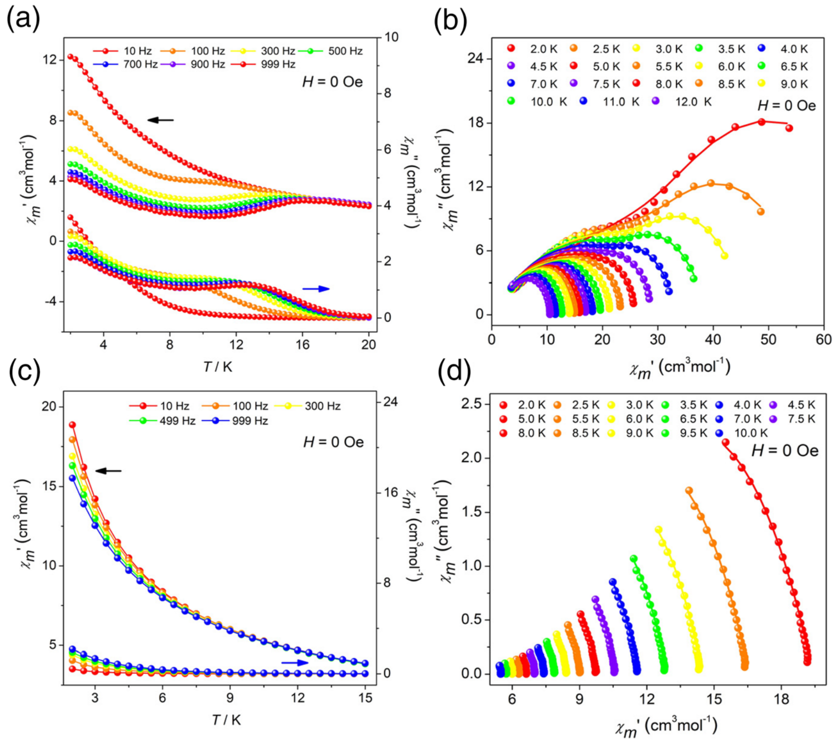

Fig. 5 Temperature-dependent χ' and χ'' AC susceptibilities under 0 Oe dc fields for ***R*-1** (a) and ***R*-2** (c); and Cole–Cole plots for ***R*-1** (b) and ***R*-2** (d).

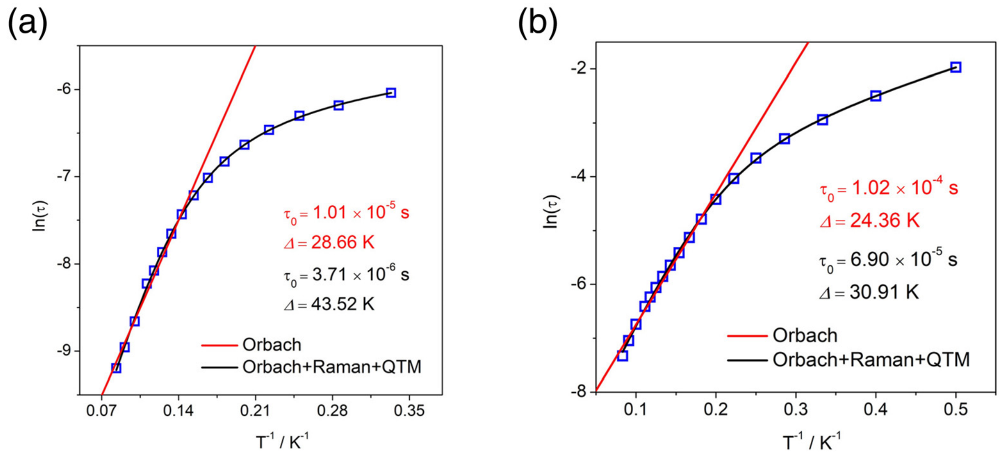

Fig. 6 Arrhenius plots generated from the temperature-dependent relaxation times extracted from the Cole–Cole fits of the AC susceptibilities for the cluster ***R*-1** under 0 Oe dc field (a and b). Symbols show the extracted times, and the lines are least-squares fits.

exhibiting double relaxation processes, namely the fast relaxation phase (FR, with a relatively short relaxation time) and the slow relaxation phase (SR, with a relatively long relaxation time) (Fig. 5b and S10b†).[29,48] The $\ln(\tau/s)$ *vs.* T^{-1} curve for the cluster ***R*-1** was also plotted from these fitting results. The temperature-dependent relaxation time was analyzed by assuming the thermal activation process according to the Arrhenius law $\tau = \tau_0 \exp(U_{\text{eff}}/k_BT)$. At high temperatures, we applied an Orbach relaxation process ($\tau^{-1} = \tau_0{}^{-1} \exp(-U_{\text{eff}}/k_BT)$ to best fit obtained $U_{\text{eff}} = 28.66$ K, $\tau_0 = 1.01 \times 10^{-5}$ s for the FR phase (Fig. 6a) and $U_{\text{eff}} = 24.36$ K, $\tau_0 = 1.02 \times 10^{-4}$ s for the SR phase (Fig. 6b), respectively. In addition, in order to adapt to a larger temperature range, the fitting process should include multiple relaxation processes, such as the Orbach process ($\tau_0{}^{-1} \exp(-U_{\text{eff}}/k_BT)$), Raman ($CT^n$), direct relaxation process (AH^mT) and quantum tunneling process (QTM); the direct relaxation process can be ignored for the slow relaxation behaviors at zero field. So, we considered multinomial relaxation processes ($\tau^{-1} = \tau_0{}^{-1} \exp(-U_{\text{eff}}/k_BT) + \tau_{\text{QTM}}{}^{-1} + CT^n$) to fit ***R*-1** over all of the temperatures, and we obtained $U_{\text{eff}} = 43.52$ K, $\tau_0 = 3.71 \times 10^{-6}$ s for the FR phase (Fig. 6a) and $U_{\text{eff}} = 30.91$ K, $\tau_0 = 6.90 \times 10^{-5}$ s for the SR phase (Fig. 6b), respectively.[49,50] The Cole–Cole plots for the ***R*-2** at 0 Oe and 1000 Oe dc fields are shown in Fig. 5d and S7d;† since the ***R*-2** had no field effect, it cannot be fitted. Magnetic analysis showed that ***R*-1** had more obvious SMM behavior than ***R*-2**. The $\ln(\tau/s)$ *vs.* T^{-1} curve for the cluster ***S*-1** is shown in Fig. S12a and S12b.†

Conclusion

In summary, we induced the formation of template units with different linkages through the change of hydroxyl coordination sites at different positions on the ligands and realized the directional construction of two pairs of chiral lanthanide clusters ***R*/*S*-1** and ***R*/*S*-2** with different shapes and magnetic properties by hydrolysis manipulating the annular growth mechanism. The template unit formed in the initial stage of the reaction is crucial for the design and synthesis of chiral clusters. Two HL^1 ligands co-chelate one Dy(III) ion to form a mononuclear template unit $Dy(L_1)^2$. The above template units are pulled by a bridge anion μ_4-O^{2-} and assembled to form square-shaped clusters ***R*/*S*-1** through the annular growth mechanism. The change of the hydroxyl coordination sites enables the H_3L^2 ligand to capture two Dy(III) ions and to form the template unit Dy_2L^2. The above three Dy_2L^2 are assembled along the annular arrangement by the traction of the bridge anion μ_3-OH^- to form triangular pyramidal hexanuclear clusters ***R*/*S*-2**. Magnetic studies showed that the chiral clusters ***R*-1** and ***S*-1** exhibited obvious single-molecule magnet behavior with double relaxation behavior under zero dc field. To the best of our knowledge, this is one of the rare examples of chiral lanthanide clusters with double relaxation behavior. The ***R*-2** and ***S*-2** have distinct frequency-dependent behavior under zero dc field. This work provides a vivid example for the design and synthesis of chiral lanthanide clusters, and for the first time, the self-assembly process is regulated by the design of coordination sites to induce the formation of chiral lanthanide clusters with different shapes. Furthermore, this work opens a door for the directional construction of specific chiral clusters, which opens a new horizon for the design and synthesis of multifunctional materials with magneto-optical applications.

Conflicts of interest

There are no conflicts to declare.

Acknowledgements

This work was supported by the National Natural Science Foundation of China (22075058 and 22061005).

References

1 P. Peluso and B. Chankvetadze, Recognition in the Domain of Molecular Chirality: From Noncovalent Interactions to Separation of Enantiomers, *Chem. Rev.*, 2022, **122**, 13235–13400.

2 D. P. Glavin, A. S. Burton, J. E. Elsila, J. C. Aponte, J. C. Aponte and J. P. Dworkin, The Search for Chiral Asymmetry as a Potential Biosignature in our Solar System, *Chem. Rev.*, 2020, **120**, 4660–4689.

3 X. L. Zhao, S. Q. Zang and X. Y. Chen, Stereospecific interactions between chiral inorganic nanomaterials and biological systems, *Chem. Soc. Rev.*, 2020, **49**, 2481–2503.

4 G. Z. Kong, M. Y. Xiong, L. Liu, L. Hu, H.-M. Meng, G. L. Ke, X.-B. Zhang and W. H. Tan, DNA origami-based protein networks: from basic construction to emerging applications, *Chem. Soc. Rev.*, 2021, **50**, 1846–1873.

5 M. S. Xiao, W. Lai, T. T. Man, B. B. Chang, L. Li, A. R. Chandrasekaran and H. Pei, Rationally Engineered Nucleic Acid Architectures for Biosensing Applications, *Chem. Rev.*, 2019, **119**, 11631–11717.

6 F. De Fazio, D. Misatziou, Y. R. Baker, O. L. Muskens, T. Brown and A. G. Kanaras, Chemically modified nucleic acids and DNA intercalators as tools for nanoparticle assembly, *Chem. Soc. Rev.*, 2021, **50**, 13410–13440.

7 G. X. Y. Huang, X. C. Zhan, C. Zeng, K. Liang, X. C. Zhu, Y. Y. Zhao, P. Wang, Q. F. Wang, Q. Zhou, Q. H. Tao, M. H. Liu, J. L. Lei, C. Y. Yan and Y. G. Shi, Cryo-EM structure of the inner ring from the Xenopus laevis nuclear pore complex, *Cell Res.*, 2022, **32**, 451–460.

8 R. Bai, R. X. Wan, L. Wang, K. Xu, Q. F. Zhang, J. L. Lei and Y. G. Shi, Structure of the activated human minor spliceosome, *Science*, 2021, **371**, 1220.

9 X. C. Zhu, G. X. Y. Huang, C. Zeng, X. C. Zhan, K. Liang, Q. K. Xu, Y. Y. Zhao, P. Wang, Q. F. Wang, Q. Zhou, Q. H. Tao, M. H. Liu, J. L. Lei, C. Y. Yan and Y. G. Shi, Structure of the cytoplasmic ring of the Xenopus laevis nuclear pore complex, *Science*, 2022, **376**, 1177.

10 X.-Z. Li, C.-B. Tian and Q.-F. Sun, Coordination-Directed Self-Assembly of Functional Polynuclear Lanthanide Supramolecular Architectures, *Chem. Rev.*, 2022, **122**, 6374–6458.

11 S.-J. Hu, X.-Q. Guo, L.-P. Zhou, D.-N. Yan, P.-M. Cheng, L.-X. Cai, X.-Z. Li and Q.-F. Sun, Guest-Driven Self-Assembly and Chiral Induction of Photofunctional Lanthanide Tetrahedral Cages, *J. Am. Chem. Soc.*, 2022, **144**, 4244–4253.

12 Y. Y. Zhou, H. F. Li, T. Y. Zhu, T. Gao and P. F. Yan, A Highly Luminescent Chiral Tetrahedral $Eu_4L_4(L')_4$ Cage: Chirality Induction, Chirality Memory, and Circularly Polarized Luminescence, *J. Am. Chem. Soc.*, 2019, **141**, 19634–19643.

13 J. J. Jiao, C. X. Tan, Z. J. Li, Y. Liu, X. Han and Y. Cui, Design and Assembly of Chiral Coordination Cages for Asymmetric Sequential Reactions, *J. Am. Chem. Soc.*, 2018, **140**, 2251–2259.

14 Y.-J. Hou, K. Wu, Z.-W. Wei, K. Li, Y.-L. Lu, C.-Y. Zhu, J.-S. Wang, M. Pan, J.-J. Jiang, G.-Q. Li and C.-Y. Su, Design and Enantioresolution of Homochiral Fe(II)-Pd(II) Coordination Cages from Stereolabile Metalloligands: Stereochemical Stability and Enantioselective Separation, *J. Am. Chem. Soc.*, 2018, **140**, 18183–18191.

15 Y. B. Tan, Y. Okayasu, S. Katao, Y. Nishikawa, F. Asanoma, M. Yamada, J. Yuasa and T. Kawai, Visible Circularly Polarized Luminescence of Octanuclear Circular Eu(III) Helicate, *J. Am. Chem. Soc.*, 2020, **142**, 17653–17661.

16 J. Wang, Z.-H. Zhu, M.-W. Chen, Q.-A. Chen and Y.-G. Zhou, Catalytic BiomimeticAsymmetric Reduction of Alkenes and Imines Enabled by Chiral and Regenerable NAD(P)H Models, *Angew. Chem., Int. Ed.*, 2019, **58**, 1813–1817.

17 K. Wang, F. Ma, D. D. Qi, X. Chen, Y. X. Chen, Y.-C. Chen, H.-L. Sun, M.-L. Tong and J. Z. Jiang, Chiral bis(phthalocyaninato) terbium double-decker compounds with enhanced single-ion magnetic behavior, *Inorg. Chem. Front.*, 2018, **5**, 939–943.

18 Z. H. Zhu, C. Zhao, T. T. Feng, X. D. Liu, X. Ying, X.-L. Li, Y.-Q. Zhang and J. K. Tang, Air-Stable Chiral Single-Molecule Magnets with Record Anisotropy Barrier Exceeding 1800 K, *J. Am. Chem. Soc.*, 2021, **143**, 10077–10082.

19 C. X. Tan, J. J. Jiao, Z. J. Li, Y. Liu, X. Han and Y. Cui, Design and Assembly of a Chiral Metallosalen-Based Octahedral Coordination Cage for Supramolecular Asymmetric Catalysis, *Angew. Chem., Int. Ed.*, 2018, **57**, 2085–2090.

20 C. F. Zhu, H. T. Tang, K. K. Yang, Y. Fang, K.-Y. Wang, Z. F. Xiao, X. Wu, Y. G. Li, J. A. Powell and H.-C. Zhou, Homochiral Dodecanuclear Lanthanide "Cage in Cage" for Enantioselective Separation, *J. Am. Chem. Soc.*, 2021, **143**, 12560–12566.

21 J. H. Zhang, L. X. Dai, A. M. Webster, W. T. K. Chan, L. E. Mackenzie, R. Pal, S. L. Cobb and G.-L. Law, Unusual Magnetic Field Responsive Circularly Polarized Luminescence Probes with Highly Emissive Chiral Europium(III) Complexes, *Angew. Chem., Int. Ed.*, 2021, **60**, 1004–1010.

22 X. Wang, S.-Q. Wang, J.-N. Chen, J.-H. Jia, C. Wang, K. Paillot, I. Breslavetz, L.-S. Long, L.-S. Zheng, G. L. J. A. Rikken, C. Train, X.-J. Kong and M. Atzori, Magnetic 3d-4f Chiral Clusters Showing Multimetal Site Magneto-Chiral Dichroism, *J. Am. Chem. Soc.*, 2022, **144**, 8837–8847.

23 F. Gendron, S. Di Pietro, L. Abad Galán, F. Riobé, V. Placide, L. Guy, F. Zinna, L. Di Bari, A. Bensalah-Ledoux, Y. Guyot, G. Pilet, F. Pointillart, B. Baguenard, S. Guy, O. Cador, O. Maury and B. Le Guennic, Luminescence, chiroptical, magnetic and ab initio crystal-field characterizations of an enantiopure helicoidal Yb(III) complex, *Inorg. Chem. Front.*, 2021, **8**, 914–926.

24 M. Feng, B.-H. Lyu, M.-H. Wang, W.-W. Wu, Y.-C. Chen, G.-Z. Huang, W.-Q. Lin, S.-G. Wu, J.-L. Liu and M.-L. Tong,

Chiral Erbium(III) Complexes: Single-Molecule Magnet Behavior, Chirality, and Nuclearity Control, *Inorg. Chem.*, 2019, **58**, 10694–10703.

25 M.-H. Du, L.-Q. Chen, L.-P. Jiang, W.-D. Liu, L.-S. Long, L.-S. Zheng and X.-J. Kong, Counterintuitive Lanthanide Hydrolysis-Induced Assembly Mechanism, *J. Am. Chem. Soc.*, 2022, **144**, 5653–5660.

26 H. Zheng, M.-H. Du, S.-C. Lin, Z.-C. Tang, X.-J. Kong, L.-S. Long and L.-S. Zheng, Assembly of a Wheel-Like $Eu_{24}Ti_8$ Cluster under the Guidance of High-Resolution Electrospray Ionization Mass Spectrometry, *Angew. Chem., Int. Ed.*, 2018, **57**, 10976–10979.

27 W. M. Huang, W. M. Chen, Q. X. Bai, Z. Zhang, M. Feng and Z. P. Zheng, Anion-Guided Stepwise Assembly of High-Nuclearity Lanthanide Hydroxide Clusters, *Angew. Chem., Int. Ed.*, 2022, **61**, e202205385.

28 Z.-H. Zhu, X.-F. Ma, H.-L. Wang, H.-H. Zou, K.-Q. Mo, Y.-Q. Zhang, Q.-Z. Yang, B. Li and F.-P. Liang, A triangular Dy_3 single-molecule toroic with high inversion energy barrier: magnetic properties and multiple-step assembly mechanism, *Inorg. Chem. Front.*, 2018, **5**, 3155–3162.

29 H.-L. Wang, X.-F. Ma, J.-M. Peng, Z.-H. Zhu, B. Li, H.-H. Zou and F.-P. Liang, Tracking the Stepwise Formation of the Dysprosium Cluster (Dy_{10}) with Multiple Relaxation Behavior, *Inorg. Chem.*, 2019, **58**, 9169–9174.

30 Z.-R. Luo, H.-L. Wang, Z.-H. Zhu, T. Liu, X.-F. Ma, H.-F. Wang, H.-H. Zou and F.-P. Liang, Assembly of Dy_{60} and Dy_{30} cage-shaped nanoclusters, *Commun. Chem.*, 2020, **3**, 1–9.

31 Z.-H. Zhu, J.-M. Peng, H.-L. Wang, H.-H. Zou and F.-P. Liang, Assembly Mechanism and Heavy Metal Ion Sensing of Cage-Shaped Lanthanide Nanoclusters, *Cell Rep. Phys. Sci.*, 2020, **1**, 100165.

32 H.-L. Wang, T. Liu, Z.-H. Zhu, J.-M. Peng, H.-H. Zou and F.-P. Liang, A series of dysprosium clusters assembled by a substitution effect-driven out-to-in growth mechanism, *Inorg. Chem. Front.*, 2021, **8**, 2136–2143.

33 Y.-L. Li, H.-L. Wang, Z.-H. Zhu, F.-P. Liang and H.-H. Zou, Giant Crown-Shaped Dy_{34} Nanocluster with High Acid-Base Stability Assembled by an out-to-in Growth Mechanism, *Inorg. Chem.*, 2022, **61**, 10101–10107.

34 Z.-R. Luo, H.-H. Zou, Z.-L. Chen, B. Li, K. Wang and F.-P. Liang, Triethylamine-templated nanocalix Ln_{12} clusters of diacylhydrazone: crystal structures and magnetic properties, *Dalton Trans.*, 2019, **48**, 17414–17421.

35 Y.-L. Li, H.-L. Wang, Z.-H. Zhu, J. Li, H.-H. Zou and F.-P. Liang, A Series of High-Nuclear Gadolinium Cluster Aggregates with a Magnetocaloric Effect Constructed through Two-Component Manipulation, *Inorg. Chem.*, 2021, **60**, 16794–16802.

36 K.-Q. Mo, Z.-H. Zhu, H.-L. Wang, X.-F. Ma, J.-M. Peng, H.-H. Zou, J. Bai and F.-P. Liang, Substituents lead to differences in the formation of two different butterfly-shaped $Ni^{II}_2Dy^{III}_2$ clusters: structures and multistep assembly mechanisms, *Dalton Trans.*, 2019, **48**, 16641–16649.

37 H.-L. Wang, J.-M. Peng, Z.-H. Zhu, K.-Q. Mo, X.-F. Ma, B. Li, H.-H. Zou and F.-P. Liang, Step-by-Step and Competitive Assembly of Two Dy(III) Single-Molecule Magnets with Their Performance Tuned by Schiff Base Ligands, *Cryst. Growth Des.*, 2019, **19**, 5369–5375.

38 J.-M. Peng, H.-L. Wang, Z.-H. Zhu, J. Bai, F.-P. Liang and H.-H. Zou, Series of the Largest Dish-Shaped Dysprosium Nanoclusters Formed by In Situ Reactions, *Inorg. Chem.*, 2022, **61**, 6094–6100.

39 S. Alvarez, P. Alemany, D. Casanova, J. Cirera, M. Llunell and D. Avnir, Shape maps and polyhedral interconversion paths in transition metal chemistry, *Coord. Chem. Rev.*, 2005, **249**, 1693–1708.

40 H.-L. Wang, T. Liu, Z.-H. Zhu, J.-M. Peng, H.-H. Zou and F.-P. Liang, pH manipulates the assembly of a series of dysprosium clusters with subtle difference, *Inorg. Chem. Front.*, 2021, **8**, 3134–3140.

41 C.-M. Liu, R. Sun, B.-W. Wang, F. Wu, X. Hao and Z. Shen, Homochiral Ferromagnetic Coupling Dy_2 Single-Molecule Magnets with Strong Magneto-Optical Faraday Effects at Room Temperature, *Inorg. Chem.*, 2021, **60**, 12039–12048.

42 M. H. Cui, L. P. Yang, F. C. Li, L. M. Zhou, Y. L. Song, S.-M. Fang, C.-M. Liu and X.-L. Li, Multifunctional Dy^{III} Enantiomeric Pairs Showing Enhanced Photoluminescences and Third-Harmonic Generation Responses through the Coordination Role of Homochiral Tridentate N,N,N- Pincer Ligands, *Inorg. Chem.*, 2021, **60**, 13366–13375.

43 F.-S. Guo, A. K. Bar and R. A. Layfield, Main Group Chemistry at the Interface with Molecular Magnetism, *Chem. Rev.*, 2019, **119**, 8479–8505.

44 J. Liu, Y.-C. Chen, J.-L. Liu, V. Vieru, L. Ungur, J.-H. Jia, L. F. Chibotaru, Y. Lan, W. Wernsdorfer, S. Gao, X.-M. Chen and M.-L. Tong, A Stable Pentagonal Bipyramidal Dy(III) Single-Ion Magnet with a Record Magnetization Reversal Barrier over 1000 K, *J. Am. Chem. Soc.*, 2016, **138**, 5441–5450.

45 Y.-C. Chen, J.-L. Liu, L. Ungur, J. Liu, Q.-W. Li, L.-F. Wang, Z.-P. Ni, L. F. Chibotaru, X.-M. Chen and M.-L. Tong, Symmetry-Supported Magnetic Blocking at 20 K in Pentagonal Bipyramidal Dy(III) Single-Ion Magnets, *J. Am. Chem. Soc.*, 2016, **138**, 2829–2837.

46 Y.-N. Guo, G.-F. Xu, W. Wernsdorfer, L. Ungur, Y. Guo, J.-K. Tang, H.-J. Zhang, L. F. Chibotaru and A. K. Powell, Strong Axiality and Ising Exchange Interaction Suppress Zero-Field Tunneling of Magnetization of an Asymmetric Dy_2 Single-Molecule Magnet, *J. Am. Chem. Soc.*, 2011, **133**, 11948–11951.

47 P. Zhang, L. Zhang, C. Wang, S. F. Xue, S.-Y. Lin and J. K. Tang, Equatorially Coordinated Lanthanide Single Ion Magnets, *J. Am. Chem. Soc.*, 2014, **136**, 4484–4487.

48 J. F. Wu, S.-Y. Lin, S. Shen, X.-L. Li, L. Zhao, L. Zhang and J. K. Tang, Probing the magnetic relaxation and magnetic moment arrangement in a series of Dy_4 squares, *Dalton Trans.*, 2017, **46**, 1577–1584.

49 Z.-H. Zhu, H.-F. Wang, S. Yu, H.-H. Zou, H.-L. Wang, B. Yin and F.-P. Liang, Substitution Effects Regulate the Formation of Butterfly-Shaped Tetranuclear Dy(III) Cluster and Dy-Based Hydrogen-Bonded Helix Frameworks: Structure and Magnetic Properties, *Inorg. Chem.*, 2020, **59**, 11640–11650.

50 H.-F. Wang, Z.-H. Zhu, J.-M. Peng, B. Yin, H.-L. Wang, H.-H. Zou and F.-P. Liang, Multifunctional Binuclear Ln(III) Complexes Obtained via In Situ Tandem Reactions: Multiple Photoresponses to Volatile Organic Solvents and Anticounterfeiting and Magnetic Properties, *Inorg. Chem.*, 2020, **59**, 13774–13783.